Super-Resolution Mapping of Reactive Sites on Titania-Based Nanoparticles with Water-Soluble Fluorogenic Probes

Takashi Tachikawa,* Tomoyuki Yonezawa, and Tetsuro Majima*

The Institute of Scientific and Industrial Research (SANKEN), Osaka University, Mihogaoka 8-1, Ibaraki, Osaka 567-0047, Japan

ABSTRACT Interfacial charge transfer at the heterogeneous surface of semiconductor nanoparticles is a fundamental process that is relevant to many important applications, such as photocatalysis, solar cells, and sensors. In this study, we developed new water-soluble fluorogenic probes for interfacial electron transfer reactions on semiconductor nanoparticles. The synthesized boron-dipyrromethene-based fluorescence dyes have one or two sulfonate groups, which confer solubility in aqueous media, and a dinitrophenyl group as a redox reaction site. These probes produce the corresponding fluorescent products *via* multiple interfacial electron transfer processes, allowing us to investigate the photoinduced redox reactions over individual pristine and Au-nanoparticle-deposited TiO_2 nanoparticles at the single-particle, single-molecule levels. The minimum probe concentration to detect single-product molecules on a single TiO_2 nanoparticle was found to be in the nanomolar range (<10 nM) in acidic solution. Furthermore, super-resolution mapping of the reaction sites revealed that visible-light-induced reduction reactions preferentially occurred on the TiO_2 surface within a distance of a few tens of nanometers around the deposited Au nanoparticles. This result was qualitatively interpreted on the basis of plasmon-induced electron and/or energy transfer mechanisms. Overall, this study provides a great deal of valuable information related to solar-energy-conversion processes that is impossible or difficult to obtain from ensemble-averaged experiments.

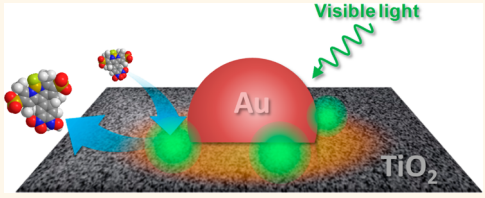

KEYWORDS: electron transfer · fluorogenic probe · single-molecule fluorescence spectroscopy · surface plasmon resonance · TiO_2 nanoparticle

There is significant current interest in the development of molecular probes for the characterization of chemical, biological, and physical processes in nanoscale environments.[1−5] For instance, fluorogenic probes are non-emissive molecules which become highly emissive after interacting or reacting with a substance of interest.[6,7] Synthetic fluorogenic probes have been designed based on various concepts, including energy transfer, electron transfer (ET), and heavy atom effects. Because of their high sensitivities and specificities, they have been used both *in vitro* and *in vivo* to detect biologically relevant targets, such as metal ions and reactive oxygen species. Recently, such probes have been successfully applied at high spatial and temporal resolutions in the exploration of chemical reactions occurring on heterogeneous catalysts,[8−12] for example, layered double hydroxides,[13,14] metal nanoparticles,[15−18] carbon nanotubes,[19] titanium dioxide (TiO_2),[20−25] and synthetic zeolites,[26,27] using the rapidly developing technology of single-molecule fluorescence spectroscopy. In particular, the high-resolution reconstruction method, which is based on the catalytic conversion of fluorogenic substrates, has been applied in the identification of catalytic sites beyond the optical diffraction limit (a few hundred nanometers in the lateral direction).[18,19,26]

Interfacial ET on semiconductor or metal nanostructures governs their optoelectronic and catalytic performances; thus, a proper understanding of the ET mechanism can provide helpful information for the design of highly efficient devices. Very recently, we designed and synthesized a novel redox-responsive boron-dipyrromethene (BODIPY) fluorescent probe, 3,4-dinitrophenyl-BODIPY (DN-BODIPY, Figure 1), on the basis of a photoinduced intramolecular ET mechanism.[21] DN-BODIPY is composed of a BODIPY fluorophore and a reactive dinitrophenyl group. BODIPYs are promising dyes for bioimaging applications because of their attractive properties, such as high extinction coefficients (ε), high fluorescence quantum yields (Φ_{fl}), good chemical and photostabilities, and

* Address correspondence to tachi45@sanken.osaka-u.ac.jp, majima@sanken.osaka-u.ac.jp.

Received for review August 29, 2012 and accepted December 5, 2012.

Published online December 05, 2012
10.1021/nn303964v

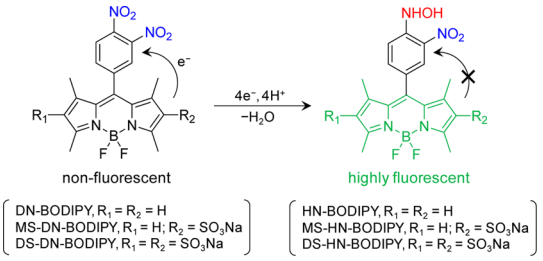

Figure 1. Generation of highly fluorescent products from nonfluorescent probes.

their facile chemical modification.[28,29] The reduction of nitro groups to nitroso, hydroxylamino, and, eventually, amino groups has been chosen as the model reaction to evaluate the catalytic performance of semiconductor and metal nanoparticles.[30−33] Prior to the reduction, the two nitro groups greatly reduce the lowest unoccupied molecular orbital (LUMO) energy level of the benzene moiety at the *meso*-position of the BODIPY core because of their strong electron-withdrawing nature. As a result, fluorescence is strongly quenched by an intramolecular ET from the excited BODIPY to the dinitrophenyl group. Upon the reduction of one nitro group to the electron-donating hydroxylamino group, fluorescence quenching is significantly suppressed as a result of the greatly increased highest occupied molecular orbital (HOMO) energy level of the benzene moiety.

TiO_2 photocatalytic reactions are basically initiated by band gap excitation with UV light irradiation (λ < 390 nm for anatase) to generate a number of electrons (e^-) and holes (h^+) in the conduction band (CB) and valence band (VB), respectively.[34−37] These charge carriers can react with molecules adsorbed on the TiO_2 surface, thus acting as catalysts. Both ensemble-averaged and single-molecule fluorescence experiments have demonstrated that DN-BODIPY acts as a highly sensitive fluorogenic probe to monitor the photoinduced ET process on a single TiO_2 nanoparticle in methanol solutions.[21] However, the experimental conditions are limited by the poor solubility of DN-BODIPY in water (<100 nM) and its weak adsorption onto the catalyst surface. Photocatalytic hydrogen evolution from water is attractive as a means of converting solar energy into chemical energy and has been the subject of much interest.[38−41] Thus, there is a tremendous need to develop water-soluble, ultrasensitive fluorogenic probes for the exploration of interfacial ET processes in heterogeneous catalysis.

In this study, we developed two new water-soluble compounds in the DN-BODIPY family, which have one or two sulfonate groups on the BODIPY fluorophore. The corresponding fluorescent products are generated *via* multiple interfacial ET processes upon UV irradiation of TiO_2 in analogy with the case of DN-BODIPY. The probe concentration for the detection of single-product molecules on a single TiO_2 nanoparticle can be reduced to 10 nM in acidic solution, which is more than 2 orders of magnitude lower than that of unmodified DN-BODIPY. Furthermore, the super-resolution mapping of visible-light-induced reduction reactions on Au-nanoparticle-deposited TiO_2 (Au/TiO_2) revealed that the reactive sites were spatially distributed within a distance of a few tens of nanometers from the deposited Au nanoparticles.

TABLE 1. Fluorescence Properties of Dyes in Different Solvents

dye	solvent	λ_{abs}^{max}, nm	λ_{fl}^{max}, nm	Φ_{fl}[c]	τ_{fl}[d]
DN-BODIPY	water[a]	n/a	n/a	n/a	n/a
	methanol	505	523	<0.001	<0.1[e]
	water—methanol[b]	507	527		
HN-BODIPY	water[a]	n/a	n/a	n/a	n/a
	methanol	499	510	0.50	3.7
	water—methanol[b]	500	512	0.59	4.0
MS-DN-BODIPY	water	500	522	<0.001	<0.1[e]
	methanol	507	524		
	water—methanol	508	527		
MS-HN-BODIPY	water	494	507	0.55	3.5
	methanol	500	513	0.52	3.5
	water—methanol	502	515	0.50	3.6
DS-DN-BODIPY	water	506	524	<0.001	<0.1[e]
	methanol	511	531		
	water—methanol	513	530		
DS-HN-BODIPY	water	498	510	0.31	3.1
	methanol	504	517	0.42	3.5
	water—methanol	504	522	0.54	3.7

[a] 0.1 M phosphate buffer (pH 7.4). [b] Mixture of acidic water (pH 2, $HClO_4$) (10 vol %) and methanol (90 vol %). [c] Calculated with fluorescein as fluorescence standard (Φ_{fl} = 0.85 in 0.1 N $NaOH_{aq}$). Errors are within 20%. [d] Errors are within 5%. [e] Within IRF.

RESULTS AND DISCUSSION

Newly synthesized mono- and disulfonated derivatives of DN-BODIPY are abbreviated as MS-DN-BODIPY and DS-DN-BODIPY, respectively. Their molecular structures are shown in Figure 1. The fluorescence properties of the dyes are also listed in Table 1. Both dyes are nonfluorescent in polar solvents before the reduction of the nitro group (Φ_{fl} < 0.001).

The performance of the fluorogenic probes was first examined by evaluating the photoreduction activity of TiO_2 nanoparticles (50−300 nm particle size) with ensemble-averaged absorption and fluorescence spectroscopies. When TiO_2 dispersions containing DS-DN-BODIPY (1 μM, in an Ar-saturated mixed solvent of acidic water (pH 2, $HClO_4$, 10 vol %) and methanol (90 vol %) (hereafter denoted by "aqueous methanol")) were exposed to 365 nm UV light (35 mW cm^{-2}) from a mercury lamp, a new fluorescence peak appeared at *ca.* 510 nm, and its intensity gradually increased with increasing UV irradiation time (Figure 2A). In control experiments, the increase in fluorescence intensity was negligible when the suspension was not irradiated with UV light or no TiO_2 nanoparticle was added to the

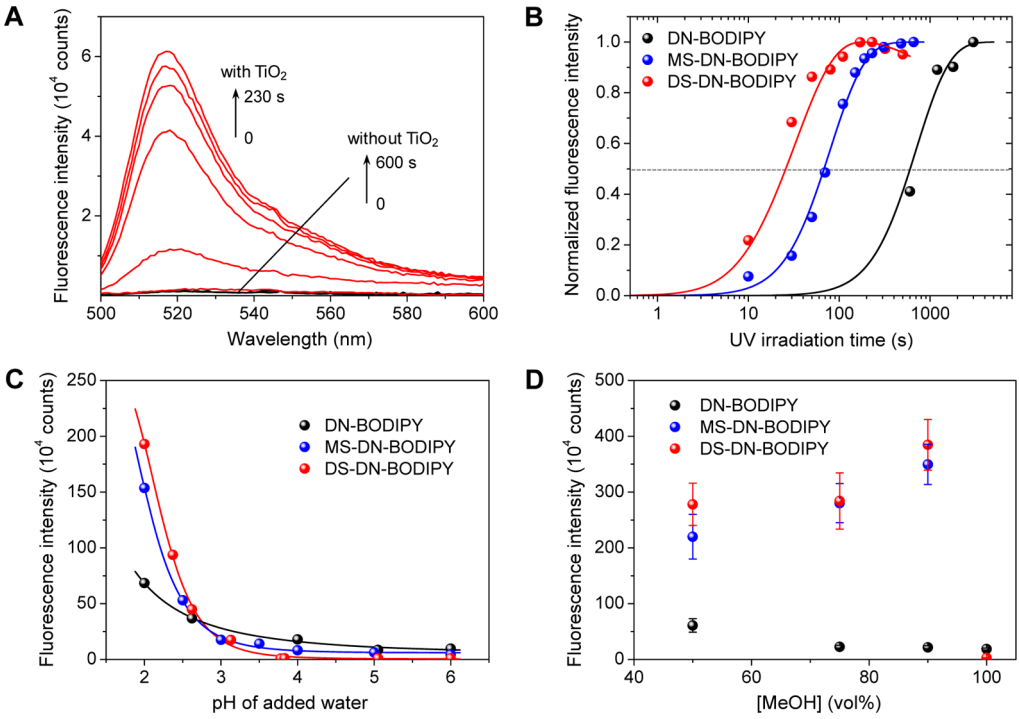

Figure 2. (A) Fluorescence spectra of Ar-saturated aqueous methanol solutions of DS-DN-BODIPY (2 μM) before and after UV irradiation in the presence and absence of TiO_2 particles (1.0 g L^{-1}). (B) UV irradiation time dependence of normalized fluorescence intensity for DN-BODIPY, MS-DN-BODIPY, and DS-DN-BODIPY. (C) pH dependence of the fluorescence intensity of the sample solutions after UV irradiation ([S] = 2 μM, [TiO_2] = 1.0 g L^{-1}). The $HClO_4$ aqueous solutions with different pH values were mixed with the same amount of methanol, and the mixtures were used as the solvent. Error was within 20%. (D) Methanol concentration dependence of the fluorescence intensity of the sample solutions after UV irradiation ([S] = 2 μM, [TiO_2] = 1.0 g L^{-1}). Different amounts of methanol were mixed with pH 2 water, and the mixtures were used as the solvent.

solution. Since the photogenerated h^+ in TiO_2 are efficiently scavenged by methanol,[37] it can be suggested that the photogenerated e^- in TiO_2 are primarily responsible for the generation of the fluorescent product. Figure 2B represents the UV irradiation time dependence of the normalized fluorescence intensity for the three probe dyes. DS-DN-BODIPY exhibited the highest rate of product formation, whereas DN-BODIPY was slowly converted to the fluorescent product over a few minutes. From the UV irradiation times ($t_{1/2}$) needed to reach the half-maximum intensity, the reaction rates ($t_{1/2}^{-1}$) were roughly estimated to be 1.6×10^{-3}, 1.5×10^{-2}, and 4.5×10^{-2} s^{-1} for DN-BODIPY, MS-DN-BODIPY, and DS-DN-BODIPY, respectively.

As shown in Figure 2C, product formation was significantly enhanced below pH 4, especially for DS-DN-BODIPY and MS-DN-BODIPY. The absorption and fluorescence properties of the BODIPY fluorophore are insensitive to the pH of the medium in the range of 2 to 12.[42,43] Since the reduction of the nitro group to the hydroxylamino group proceeds *via* a four-electron/four-proton transfer process, a lower pH of the medium should be favorable. The CB potential of anatase TiO_2 exhibits a pH dependence that decreases by 59 mV per pH unit (E_{CB} = −0.12−0.059 pH *versus* normal hydrogen electrode, NHE)[44] and, consequently, the ability of e^- to participate in redox processes decreases with decreasing pH of the medium. This tendency was not consistent with the pH dependence of the reactivity observed here. Considering that anatase TiO_2 nanoparticles usually have a point of zero charge at pH ≈ 6,[45] their surfaces will gain a positive charge at pH values lower than ~6 *via* protonation. In terms of the charge distribution, multisite complexation model,[46,47] the TiO_2 surface forms positively charged $TiOH_2^{+2/3}$ ($TiOH^{-1/3} + H^+ \leftrightarrow TiOH_2^{+2/3}$) and $Ti_2OH^{+1/3}$ ($Ti_2OH^{-2/3} + H^+ \leftrightarrow Ti_2OH^{+1/3}$) species at pH values lower than ~6, and therefore, the sulfonated probe molecules with negative charges are more readily adsorbed on the catalyst surface and the reduction reaction is favored. In fact, the equilibrium adsorption constants (K_{ad}) for DS-DN-BODIPY on TiO_2 were very sensitive to the pH values of the solutions and decreased from ~10^6 to ~10^2 M^{-1} when the pH of the added water was increased from 2 to 6 (Figure S1, Supporting Information). A similar pH dependence of molecular adsorption was observed for acid orange 7 (AO7), where the AO7 molecule was considered to be adsorbed on the TiO_2 surface *via* the two oxygen atoms of the sulfonate group of the dye.[47,48]

Figure 2D shows the methanol concentration dependence of the fluorescence intensity of the sample solutions after UV irradiation. Both sulfonated probes exhibited a dramatic increase in fluorescence intensity upon addition of 10 vol % acidic water in methanol, whereas the fluorescence intensity of DN-BODIPY after

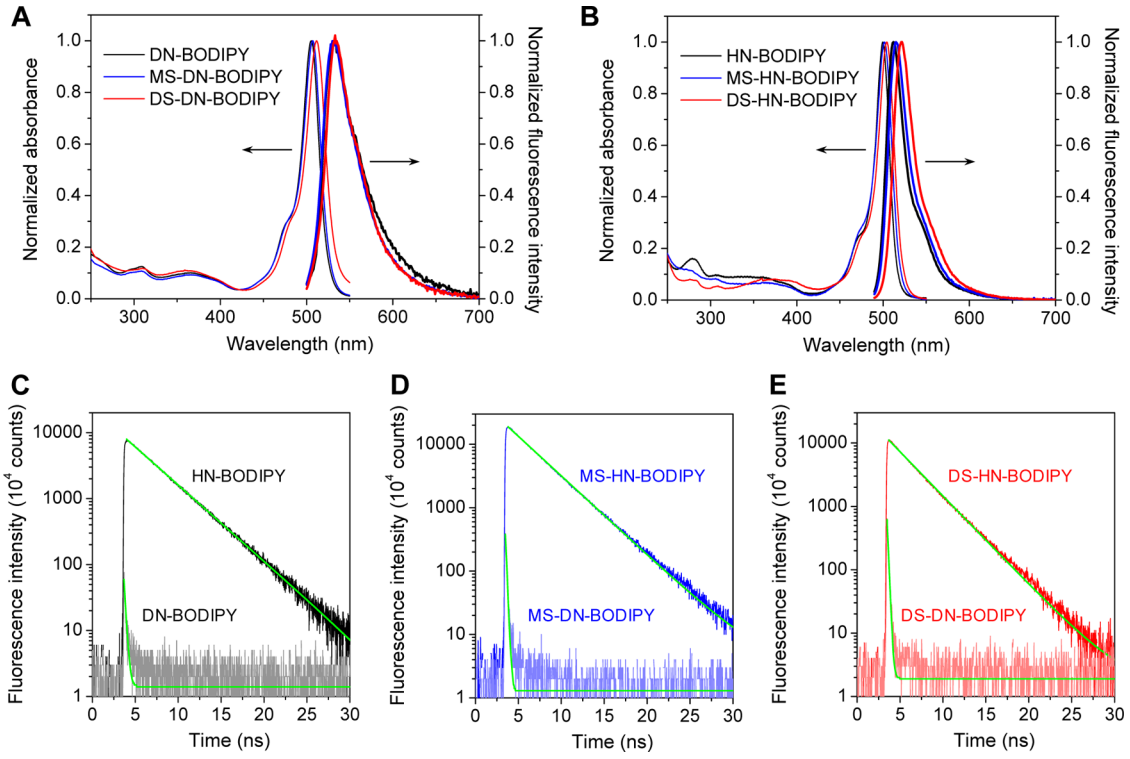

Figure 3. Normalized UV−visible absorption and fluorescence spectra of probe (A) and product (B) molecules in aqueous methanol solutions. The excitation wavelength was 470 nm. (C−E) Fluorescence decays observed for probe and product molecules in aqueous methanol solutions. The excitation wavelength was 485 nm. See Table 1 for spectral characteristics and fluorescence lifetimes.

UV irradiation was not significantly dependent on the methanol concentration. This difference is obviously caused by the greater adsorption of the sulfonated probe molecules on the positively charged TiO_2 surfaces, as discussed above.

We repeatedly purified the fluorescent products through preparative thin-layer chromatography (TLC). As previously reported, the product 4-hydroxyamino-3-nitrophenyl-BODIPY (HN-BODIPY) exhibited a high fluorescence quantum yield and a greatly prolonged fluorescence lifetime (Table 1), compared with DN-BODIPY.[21] It is thermodynamically possible that the photogenerated e^- in TiO_2 (E_{CB} = −0.88 V *vs* NHE in methanol) are transferred to the *para*-nitro group with a reduction potential of −0.54 V *vs* NHE, leading to the generation of the 4-hydroxyamino-3-nitrophenyl substituent.[49] Given that the incorporation of the two sulfonic acids in the BODIPY chromophore resulted in a small shift in its oxidation (from +1.24 to +1.21 V *vs* NHE) and reduction (−0.94 to −1.06 V *vs* NHE) potentials (Figure S2, Supporting Information), we propose the photoinduced reduction route of sulfonated DN-BODIPY over TiO_2, as illustrated in Figure 1.

Figure 3A,B depicts UV−visible absorption and fluorescence spectra of the probe and purified product molecules in aqueous methanol solutions, respectively. Also listed in Table 1 are the spectral and fluorescence properties of the probe and product molecules in 0.1 M phosphate buffer (pH 7.4), neat methanol, and water−methanol mixed solvents. The major absorption peaks of the fluorescent products were located at around 500 nm and were slightly blue-shifted by ~7 nm compared with the parent probe molecules.[50] Moreover, the fluorescent products had much higher fluorescence quantum yields (Φ_{fl} = 0.3−0.6) and longer fluorescence lifetimes (τ_{fl} = 3−4 ns) (Figure 3C−E) compared with those (Φ_{fl} < 0.001, τ_{fl} < 0.1 ns) of their parents.

We then investigated the photoinduced reduction of the probe molecules over single TiO_2 particles using wide-field fluorescence microscopy. The position and morphology of the TiO_2 particles immobilized on the cover glass were determined from the correlated optical transmission and field-emission scanning electron microscope (FE-SEM) images (Figure S4, Supporting Information).[22]

Figure 4A shows typical fluorescence images captured during the 488 nm laser irradiation of a single TiO_2 particle on the cover glass in Ar-saturated DS-DN-BODIPY (1 μM) aqueous methanol solution before and after UV irradiation (30 mW cm^{-2} at the glass surface). A sudden increase in intensity upon UV irradiation corresponds to generation of the fluorescent product (*i.e.*, DS-HN-BODIPY) (Figure 4B). The order of the fluorescence intensity increases caused by UV irradiation was similar to that of the reaction rates observed for the bulk samples (Figure 2B), that is, DS-DN-BODIPY > MS-DN-BODIPY ≫ DN-BODIPY.

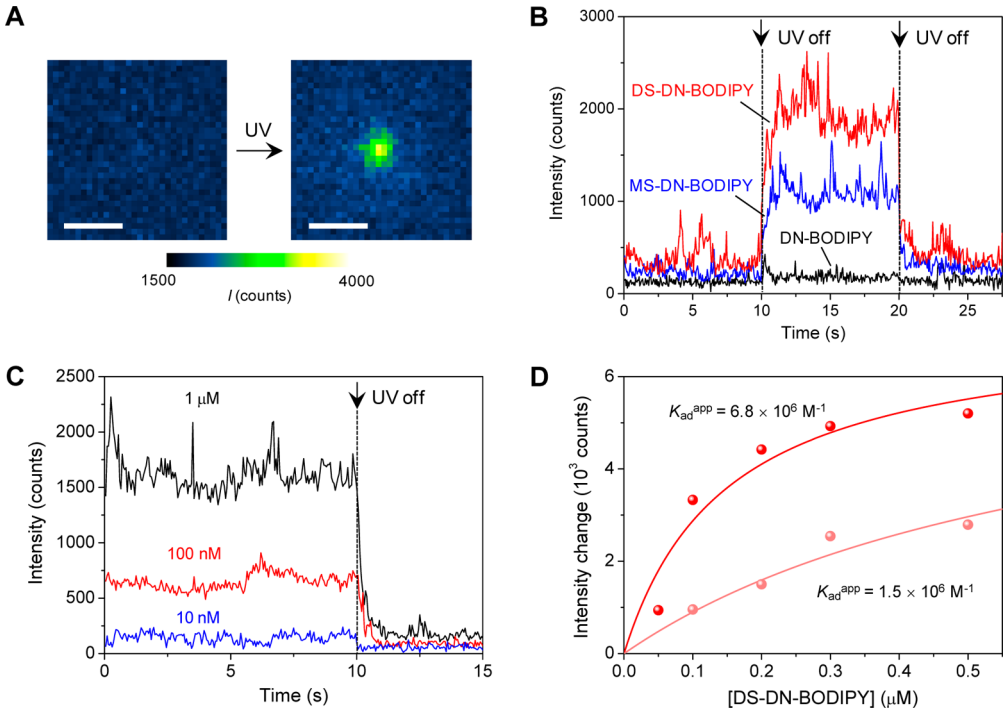

Figure 4. (A) Fluorescence images observed during the 488 nm laser irradiation of a single TiO_2 particle on the cover glass in Ar-saturated DS-DN-BODIPY (1 μM) aqueous methanol solution before and after UV irradiation. The acquisition time of an image was 50 ms. Scale bars are 1 μm. (B) Typical fluorescence intensity trajectories observed for a single TiO_2 particle in Ar-saturated aqueous methanol solutions of DN-BODIPY, MS-DN-BODIPY, and DS-DN-BODIPY (1 μM). (C) Typical fluorescence intensity trajectories observed for a single TiO_2 particle at different concentrations of DS-DN-BODIPY. (D) DS-DN-BODIPY concentration dependence of fluorescence intensity obtained for different TiO_2 particles. The solid lines were obtained from eq 1.

It should be noted that the fluorescence signals with stochastic intensity fluctuations were observed only upon 488 nm laser irradiation, especially for DS-DN-BODIPY. This is possibly attributed to the large number of adsorbed probe molecules that lead to unidentified fluorescent products from photodegradation of the probe molecules and/or defect-induced photoreduction reactions under intense laser irradiation (*vide infra*).

At higher substrate (S) concentrations, adsorption equilibrium is attained readily, thus promoting the generation of the fluorescent product (P). Figure 4C demonstrates the expected dependence of fluorescence intensity on the DS-DN-BODIPY concentration ([DS-DN-BODIPY]). The [S] dependence of the fluorescence intensity is adequately described by the Langmuir relationship:

$$\text{intensity} \propto \frac{K_{ad}^{app}[S]}{1 + K_{ad}^{app}[S]} \qquad (1)$$

where K_{ad}^{app} is the apparent equilibrium adsorption constant for S (*i.e.*, probe molecules).[24] We examined 10 different particles that exhibit varying degrees of reactivity. The resulting values of K_{ad}^{app} for each particle varied significantly, from 1.0 × 10^6 to 8.2 × 10^6 M^{-1} (Figure 4D), inferring that the heterogeneous activity among particles originates from the adsorbability of probe molecules, not simply from the difference in the number of adsorption sites and intrinsic charge separation efficiency of each particle. The average K_{ad}^{app} value (4.1 × 10^6 M^{-1}) for DS-DN-BODIPY was close to the K_{ad} value ((2 ± 1) × 10^6 M^{-1}), as determined from the ensemble-averaged experiments (Figure S1, Supporting Information); thus, the results support the validity of the model. In addition, the K_{ad}^{app} value for DS-DN-BODIPY is approximately 1 order of magnitude greater than that (0.47 × 10^6 M^{-1}) obtained for DN-BODIPY on TiO_2 in Ar-saturated methanol,[21] but this difference in K_{ad}^{app} values was unexpectedly small when compared with the difference (~30 times) in the reaction rates (Figure 2B).

At [DS-DN-BODIPY] < 10 nM, burst-like fluorescence signals appeared on single TiO_2 particles under 488 nm laser and UV irradiation (Figures 4C and 5). Similar behavior was previously observed for DN-BODIPY (0.5−2 μM) on TiO_2 in Ar-saturated methanol, and each fluorescence burst corresponded to individual product molecules.[21] In the case of DN-BODIPY, there were very limited numbers of the fluorescence bursts on TiO_2 in aqueous methanol solution. Since the reactivity of DN-BODIPY on TiO_2 was not significantly affected by the addition of acidic water in methanol, the poor reactivity observed in the single-particle experiments may be due to the lack of available photons because of fast dissociation of the product molecules from the TiO_2 surface into the bulk solution. As hydrogen

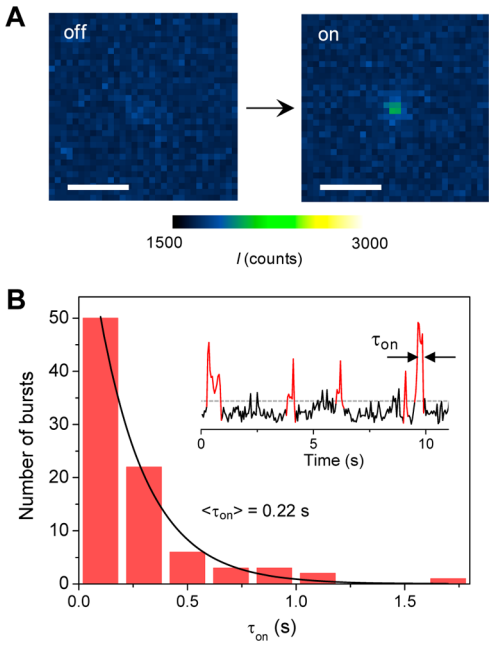

Figure 5. (A) Fluorescence images of a single TiO_2 particle on the cover glass in Ar-saturated 10 nM DS-DN-BODIPY solution under 488 nm laser and UV irradiation. The acquisition time of an image was 50 ms. Scale bars are 1 μm. (B) On-time distribution constructed for 10 different single TiO_2 particles. Inset shows a typical fluorescence intensity trajectory observed for a single TiO_2 particle in an Ar-saturated DS-DN-BODIPY solution (10 nM) under 488 nm laser and UV light irradiation. The fluorescence bursts are highlighted in red. The gray dashed line indicates the threshold level separating the on and off states.

bonding is normally stronger than molecular interactions between neutral substrate molecules (without functional groups for adsorption) and hydrated TiO_2, water molecules are likely to compete with the substrate molecules in adsorbing on the particle surface and thus inhibit the reduction reaction.[51,52] Consequently, DS-DN-BODIPY in aqueous methanol exhibited about 2 orders of magnitude higher sensitivity to the reduction reaction on a single TiO_2 particle compared to DN-BODIPY in methanol.

To further understand the molecular interaction between the product and TiO_2, we analyzed the on-time (τ_{on}) for which persistent emission was exhibited, which is related to the dissociation of fluorescent products.[21−23] As shown in Figure 5B, the distribution of τ_{on} was well fitted with a single-exponential decay function ($R^2 = 0.99$), and the average value of τ_{on} ($\langle\tau_{on}\rangle$) was determined to be 0.22 s. This value was much smaller than that for HN-BODIPY (~0.65 s) in neat methanol, thus implying that solvent water molecules assist the dissociation of product.

Multiple ET processes at the heterogeneous interface of metal/semiconductor nanocomposites have attracted a great deal of research interest because this process largely governs the photocatalytic performance for hydrogen evolution.[38−41] Here, we demonstrate that the use of DS-DN-BODIPY allows us to explore the visible-light-induced redox reactions occurring on the Au-nanoparticle-loaded TiO_2 (Au/TiO_2) particles at the single-particle, single-molecule level.

Figure 6A shows the distributions of fluorescence intensities observed for individual TiO_2 and 8 nm Au/TiO_2 particles (the number of Au nanoparticles loaded per TiO_2 particle was 10 ± 3) in Ar-saturated aqueous methanol solutions containing DS-DN-BODIPY (1 μM) under 488 nm laser irradiation (without UV light). The fluorescence intensity depended on the DS-DN-BODIPY concentration according to Langmuir−Hinshelwood-type kinetics. The determined K_{ad}^{app} values were $(1.7-8.4) \times 10^6$ M^{-1} (Figure S5, Supporting Information), which are very close to those obtained for the TiO_2 systems. In the absence of the probe molecules, emissions from both the particles on the cover glass surface were almost negligible. Therefore, the observed higher intensity on the Au/TiO_2 particles immersed in the probe solutions is probably attributable to generation of the fluorescent product (*i.e.*, DS-HN-BODIPY). Furthermore, such an emission intensity change in the presence of DS-DN-BODIPY was not observed for Au nanoparticles (Aldrich; 5, 10, and 20 nm) immobilized on the cover glass, thus suggesting that molecular adsorption of DS-DN-BODIPY on the surface of Au nanoparticles does not cause any fluorescence enhancement. This observation is consistent with the bulk experimental results that the DS-DN-BODIPY solutions with and without Au/TiO_2 particles exhibited almost the same fluorescence intensity (Figure S6, Supporting Information). On the basis of these observations, it can be inferred that (1) TiO_2 and Au nanoparticles are both necessary to form the product molecules under visible light irradiation and (2) the reduction reactions take place on the surface of TiO_2 particles.

Figure 6B shows the normalized emission spectra observed for single TiO_2 and 8 nm Au/TiO_2 particles in DS-DN-BODIPY solutions under photoirradiation. The emission spectrum observed upon 485 nm laser and UV excitation of the TiO_2 sample was identical to that of the bulk solution containing DS-HN-BODIPY, again confirming the generation of the product molecules under the present conditions. The same result was obtained for MS-DN-BODIPY. On the other hand, the emission spectrum observed upon 485 nm laser excitation of the Au/TiO_2 sample exhibited a different spectral shape. The overall spectrum was analogous to that of DS-HN-BODIPY, but the intensity in the shorter (longer) wavelength region was significantly attenuated (enhanced). Furthermore, the fluorescence decays analyzed by multiexponential functions showed that the fluorescent products generated during pulsed 485 nm laser excitation of a single Au/TiO_2 particle exhibited a slightly shorter lifetime component (0.23 ns, 90% weight), as compared with the TiO_2 sample (0.36 ns, 79% weight).[53]

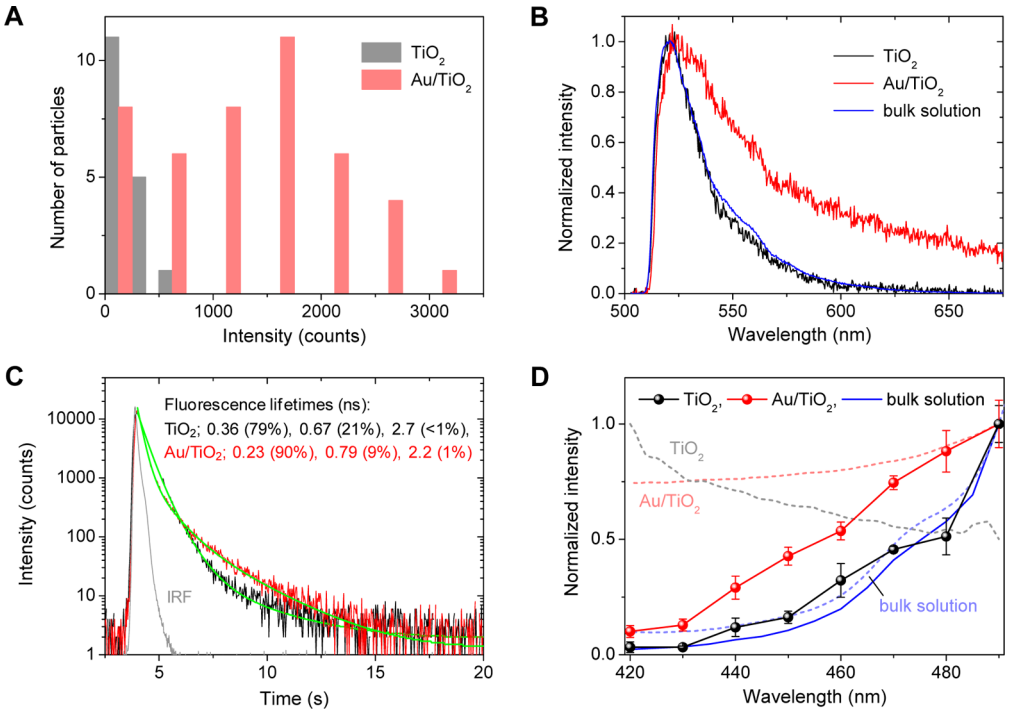

Figure 6. (A) Distribution of fluorescence intensities observed for individual TiO_2 and 8 nm Au/TiO_2 particles in Ar-saturated aqueous methanol solutions containing DS-DN-BODIPY (1 μM) under 488 nm laser irradiation. (B) Single-particle fluorescence spectra observed for TiO_2 and 8 nm Au/TiO_2 particles in Ar-saturated aqueous methanol solutions containing DS-DN-BODIPY (1 μM) under photoirradiation (at 485 and 365 nm for the TiO_2 sample and at 485 nm for the Au/TiO_2 sample). The fluorescence spectrum of the bulk solution of the product DS-HN-BODIPY is also shown. Note that the fluorescence below ~520 nm is cut off with the long-pass filter. (C) Typical fluorescence decay profiles observed during 485 and 365 nm excitation of TiO_2 and 485 nm excitation of Au/TiO_2 in Ar-saturated DS-DN-BODIPY (1 μM) solutions. Green lines indicate multiexponential curves fitted to the data. (D) Excitation spectra of the TiO_2 (solid black line) and Au/TiO_2 (solid red line) samples measured at a fixed emission wavelength of 531 nm (width 40 nm). The excitation spectrum of the bulk solution of the product DS-HN-BODIPY (solid blue line) and the absorption spectra (broken lines) of TiO_2 (gray), $AuTiO_2$ (pale red), and DS-DN-BODIPY (pale blue) are also shown.

According to the literature,[54−62] these features are indicative of fluorescence quenching and enhancement of dyes by plasmonic metal nanostructures. The detected fluorescence F emitted from the product molecules in proximity to metal nanostructures, such as Au and Ag nanoparticles, can be described as

$$F = \Gamma_{ex}(\omega_{ex})\Phi_{em}(\omega_{em})N_P(\omega_{ex})t \quad (2)$$

where $\Gamma_{ex}(\omega_{ex})$ is the excitation rate of the fluorophores at the excitation frequency ω_{ex}, $\Phi_{em}(\omega_{em})$ is the quantum yield for emission at the emission frequency ω_{em}, $N_P(\omega_{ex})$ is the number of product molecules per catalyst particle at the excitation frequency ω_{ex}, and t is the acquisition time. We neglected the collection efficiency of the light in the experimental geometry. $\Gamma_{ex}(\omega_{ex})$ depends on both the absorption cross section of the dye and the local electric field enhanced by coupling between the surface plasmon polaritons and incident light.[63,64] Recent single-particle fluorescence experiments revealed that the near-field enhancement is strongly frequency-dependent and maximizes the excitation rate near a localized surface plasmon resonance peak of the metal nanostructures.[59,60] Likewise, Φ_{em} is frequency-dependent and is defined as

$$\Phi_{em}(\omega_{em}) = \frac{\Gamma_r(\omega_{em})}{(\Gamma_r(\omega_{em}) + \Gamma_{nr}(\omega_{em}))} \quad (3)$$

where $\Gamma_r(\omega_{em})$ and $\Gamma_{nr}(\omega_{em})$ are the radiative and nonradiative rates of the fluorophores, respectively. Modification of the local photonic mode density around the fluorophore leads to changes in the radiative decay rate of the fluorophore.[63] The metal nanostructures also provide efficient nonradiative decay pathways *via* energy transfer to the metal surface.[65−69] Thus, Au nanoparticles can be attributed to either an increase or a decrease in the fluorescence quantum yield of the product molecules. In eq 2, $N_P(\omega_{ex})$ is given by

$$N_P(\omega_{ex}) = N_{ph}(\omega_{ex})\Phi_P \quad (4)$$

where $N_{ph}(\omega_{ex})$ is the number of photons absorbed by a catalyst at the excitation frequency ω_{ex}, and Φ_P is the quantum yield for product formation.

On the basis of the above arguments, significant enhancement in the radiative rate by surface plasmon coupling would be excluded by the fact that the shorter-wavelength region of the fluorescence spectrum is substantially weakened compared with the longer wavelength region (Figure 6B) despite the better spectral overlap with the surface plasmon peak

(~540 nm) of the 8 nm Au nanoparticles deposited on TiO_2 (Figure S7, Supporting Information). Thus, we can speculate that the shortening of the fluorescence lifetime on Au/TiO_2 is mainly due to energy transfer to the metal surface as an additional nonradiative process.[70] Coupling of probe and particle excitation with the surface plasmons of Au nanoparticles was further confirmed by single-particle excitation spectral measurements. The results are given in Figure 6D. For the sake of comparison, we measured the excitation spectrum of DS-HN-BODIPY generated during UV irradiation of a single TiO_2 particle in solution at a fixed emission wavelength of 531 nm (width 40 nm). The observed spectrum was very similar to the absorption and excitation spectra of DS-HN-BODIPY in the bulk solution; this suggests that the electrostatic interactions between the product molecules and TiO_2 do not strongly influence the spectral characteristics of the product molecules. On the other hand, the excitation spectrum measured for the Au/TiO_2 system without UV irradiation was much broader than those of the other two samples.

Previous studies have shown that the visible light photochemical activity of TiO_2 can be enhanced by loading with noble-metal nanostructures (mainly Au and Ag).[74,75] Thus far, the following mechanisms have been proposed: (i) photoinduced heating of metal nanoparticles,[76−78] (ii) ET from illuminated metal nanoparticles to TiO_2 mediated by surface plasmons, leaving reactive holes in the metal,[79−84] and (iii) the enhanced excitation efficiency of TiO_2 by the electromagnetic field of metal nanoparticles.[85−89] The photoinduced heating of metal nanostructures (mechanism (i)) was ruled out because no visible light photoactivity was observed for Au nanoparticles on the cover glass under the same experimental conditions.[90] Moreover, the increased local temperature inhibits the adsorption of the probe molecules on the surface, thus lowering the reaction efficiency. This explanation is supported by the dissociation rate of the product (*i.e.*, τ_{on}^{-1}) from the Au/TiO_2 particle, which was comparable to that of the TiO_2 system.[23]

Both mechanisms (ii) and (iii) would increase the concentration of e^-/h^+ pairs in the composite and lead to increased generation of product molecules. Figure 7 illustrates two possible mechanisms for the visible-light-induced reduction of the substrate on Au/TiO_2. First, upon visible light irradiation, plasmon-induced hot electrons are injected into the CB of TiO_2 over the Schottky barrier,[91] and they reduce the probe molecules on the surface, while the remaining holes in the Au nanoparticles accept electrons from solvents (water and methanol) (mechanism (ii), Figure 7A). The return of the injected electrons to the Au nanoparticles is likely to be inefficient because of the Schottky barrier at the Au/TiO_2 interface.[92] If the mechanism (ii) is dominant, the excitation spectrum for the Au/TiO_2 sample should be similar to or narrower than the absorption spectrum of the products in the examined wavelength region (see eq 2 and Figure 6D). Assuming that Φ_P is not frequency-dependent, the observed broadening of the excitation spectrum is not solely explained in terms of the electron transfer from the excited Au nanoparticles to the TiO_2 nanoparticles. As an alternative mechanism, surface plasmon excitations are converted to e^-/h^+ pairs *via* optical transitions between the localized electronic states in the band gap of the TiO_2 (mechanism (iii), Figure 7B). TiO_2 is known as a wide band gap semiconductor, but there are considerable defects in the bulk and on the surface, allowing intraband transitions by visible light illumination to generate e^-/h^+ pairs.[93,94] In fact, TiO_2 nanoparticles used in this study exhibited detectable absorption in the 400−500 nm region in addition to the UV region (Figure 6D). Therefore, the enhanced visible light activity may be partially due to surface defects on TiO_2 coupled with the localized surface plasmon of Au nanoparticles.

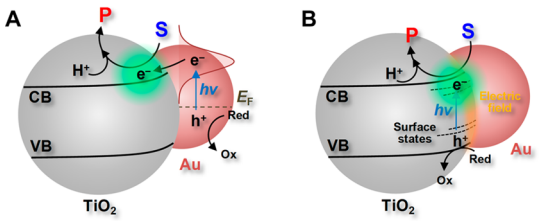

Figure 7. Proposed mechanisms of plasmon-induced photochemical reactions on Au/TiO_2. (A) Hot-electron transfer from the excited Au nanoparticles to TiO_2 nanoparticles. S and P are the substrate and fluorescent product, respectively. E_F is the Fermi energy of the Au nanoparticles. (B) Defect-mediated intraband transitions enhanced by the local electromagnetic field of the Au nanoparticles.

Since the plasmon-induced electromagnetic fields are spatially nonhomogenous and strong close to the metal nanostructures,[88,89] the formation of e^-/h^+ pairs in TiO_2 should be most effective in the vicinity of the Au nanoparticles. Furthermore, if the electromagnetic field of the Au nanoparticles creates additional accepting states at the bottom of the CB, as evidenced elsewhere,[92] the injected electrons from the excited surface plasmon states might be captured on the TiO_2 surface near the Au nanoparticles at a distance of a few tens of nanometers. The poor mobility of trapped e^- in TiO_2 compared with that of free carriers may confine the redox reactions near the Au/TiO_2 interface before spreading over the particle.[95] To examine the validity of these hypotheses, we analyzed the spatial distribution of the reactive sites over a single particle using a super-resolution microscope technique.

Figure 8C demonstrates a typical fluorescence intensity trajectory obtained for a single 14 nm Au/TiO_2 particle (the number of Au nanoparticles loaded per TiO_2 particle was 3 ± 2; see Figure 8A,B) in Ar-saturated DS-DN-BODIPY (50 nM) aqueous methanol solution

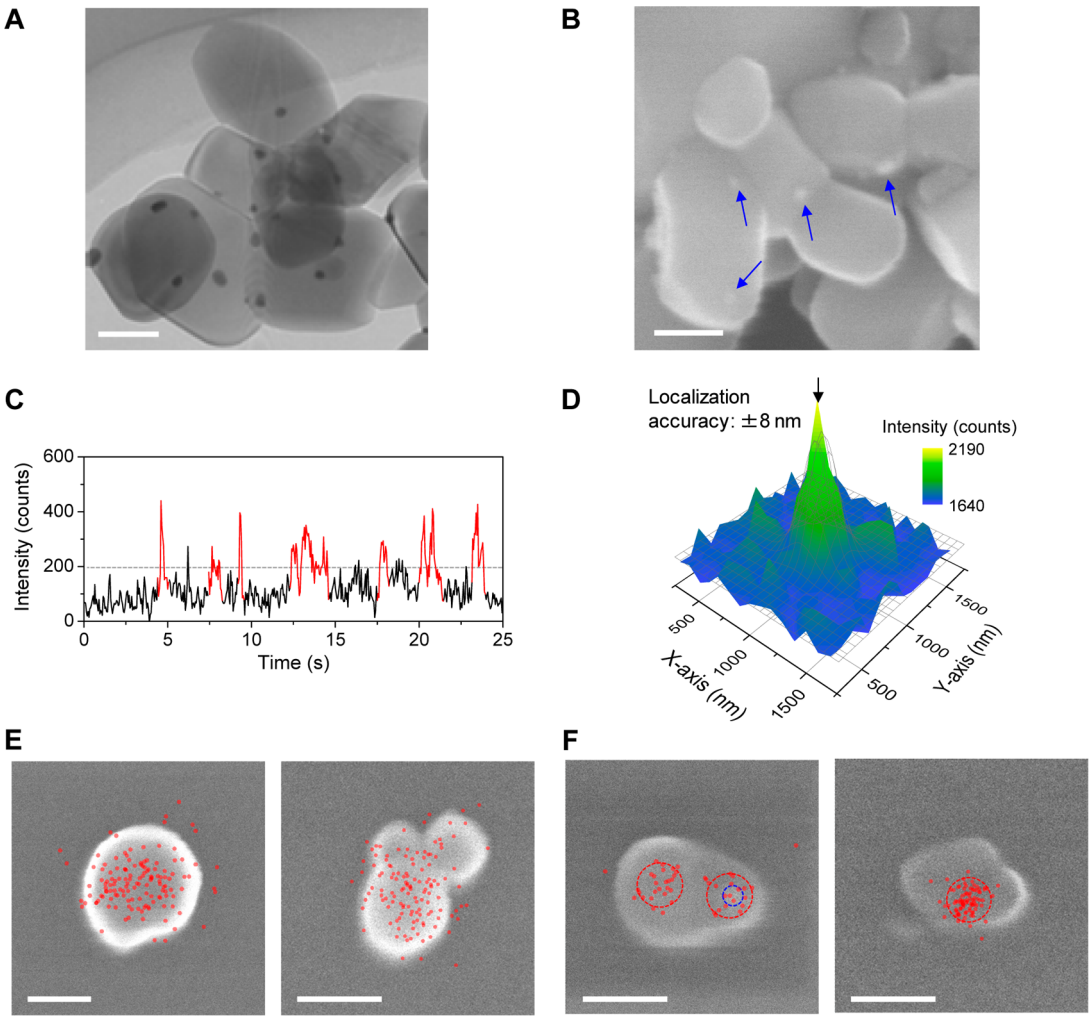

Figure 8. (A) Transmission electron microscopy (TEM) and (B) SEM images of 14 nm Au/TiO_2 particles. The scale bars are 100 nm. The blue arrows indicate the Au nanoparticles on TiO_2. (C) Typical fluorescence intensity trajectory observed for a single 14 nm Au/TiO_2 particle in an Ar-saturated DS-DN-BODIPY (50 nM) aqueous methanol solution under 488 nm laser irradiation. The fluorescence bursts are highlighted in red. The gray dashed line indicates the threshold level separating the on and off states. (D) Fluorescence intensity distribution corresponding to a single product molecule on a 14 nm Au/TiO_2 particle. To determine the centroid position, a two-dimensional Gaussian function was fitted to each image. (E,F) Spatial distributions of fluorescence spots (red dots, >50 spots) collected from TiO_2 (E) and 14 nm Au/TiO_2 particles (F). The SEM images of the particles analyzed are shown. Scale bars are 100 nm. The locations of the reactive sites and Au nanoparticle are surrounded with dashed lines in red and blue, respectively.

under 488 nm laser irradiation. A number of fluorescence bursts indicate the generation of DS-HN-BODIPY on the particle surface. The locations of the fluorescence bursts were determined with an accuracy of ~10 nm using a two-dimensional Gaussian function to the distribution of the fluorescence intensity (Figure 8D) and then overlaid on the SEM images of individual particles (or aggregates) with an accuracy of ~50 nm. For the TiO_2 system, as shown in Figure 8E, the reactive sites were almost uniformly distributed on the particle (primary particle size was 50−300 nm), which was consistent with the previous results for DN-BODIPY on TiO_2.[23] In contrast, a single 14 nm Au/TiO_2 particle exhibited a limited number of reactive centers (one or two centers) (Figure 8F), which were close to the number of Au nanoparticles loaded onto one TiO_2 particle (Figure 8A,B). Some particles exhibited the spatial correlation between the locations of the reactive sites and Au nanoparticle. Although the reactive sites were not completely assigned due to insufficient spatial resolution and limited observable surface area, quantitative super-resolution mapping of the reactive sites provided supporting evidence for plasmon-induced photochemical reactions. In the future, a combination of single-molecule fluorescence spectroscopy with several microscopic techniques such as transmission electron microscopy (TEM)[96,97] and tip-enhanced Raman microscopy[98−100] will facilitate highly spatially resolved spectroscopic analyses of interfacial ET energetics and dynamics for individual nanostructures.

CONCLUSION

In summary, we developed new water-soluble fluorogenic probes for interfacial ET reactions by

photoexcited semiconductor nanoparticles. MS-DN-BODIPY and DS-DN-BODIPY have one or two sulfonate groups on the BODIPY fluorophore, respectively, and produce the corresponding fluorescent products upon UV irradiation of TiO_2. These probes were applied to the *in situ* observation of interfacial ET events, including molecular adsorption and desorption processes at the single-particle, single-molecule level. For DS-DN-BODIPY, the minimum probe concentration to detect single-product molecules on a single TiO_2 nanoparticle was below 10 nM in acidic solution, which is 100-fold lower than that of our previous probe. Furthermore, the super-resolution mapping of visible-light-induced reduction reactions on individual Au/TiO_2 particles revealed that reactive sites were distributed over a distance of a few tens of nanometers around the deposited Au nanoparticles. This interesting finding was explained on the basis of plasmon-induced electron and/or energy transfer mechanisms. Our single-particle, single-molecule approach with ultrasensitive, water-soluble fluorogenic probes will be very useful for investigations of redox reactions in heterogeneous systems, including solid and enzymatic catalysts.

EXPERIMENTAL METHODS

Synthesis of 8-(3,4-Dinitrophenyl)-1,3,5,7-tetramethyl-4,4-difluoro-4-bora-3a,4a-diaza-*s*-indacene (DN-BODIPY). DN-BODIPY was synthesized according to literature methods.[21]

Synthesis of Sodium 2-Sulfonate-1,3,5,7-tetramethyl-8-(3,4-dinitrophenyl)-4,4-difluoro-4-bora-3a,4a-diaza-*s*-indacene (MS-DN-BODIPY). The BODIPY chromophore was sulfonated according to literature procedures.[101] In a typical synthesis, a solution of chlorosulfonic acid (20 μL, 0.30 mmol) in dry CH_2Cl_2 (2 mL) was added dropwise to a solution of DN-BODIPY (105 mg) in dry CH_2Cl_2 (25 mL) over 10 min under N_2 at −40 °C. Then, the resulting solution was slowly warmed to room temperature. After 20 min, TLC showed complete consumption of the starting material. Aqueous $NaHCO_3$ (15 mM, 20 mL) was added to neutralize the solution, and the products were separated from the CH_2Cl_2 into the aqueous layer. The aqueous layer was evaporated to dryness. The residue was purified on a silica column with 15% MeOH/CH_2Cl_2 as an eluent to afford an orange compound, MS-DN-BODIPY (52 mg, 40% yield). ^{1}H NMR (400 MHz, D_2O): δ 8.20 (d, J = 8.0 Hz, 1H), 8.18 (d, J = 11.2 Hz, 2H), 7.85 (d, J = 8.0 Hz, 1H), 6.22 (s, 1H), 2.56 (s, 3H), 2.41 (s, 3H), 1.52 (s, 3H), 1.34 (s, 3H). MS (ESI): calcd for $[M + Na]^+$, 539.06; found, 539.06.

Synthesis of Disodium 2,6-Disulfonate-1,3,5,7-tetramethyl-8-(3,4-dinitrophenyl)-4,4-difluoro-4-bora-3a,4a-diaza-s-indacene (DS-DN-BODIPY). The BODIPY chromophore was sulfonated according to literature procedures.[101] In a typical synthesis, a solution of chlorosulfonic acid (33 μL, 0.50 mmol) in dry CH_2Cl_2 (2 mL) was added dropwise to a solution of DN-BODIPY (100 mg) in dry CH_2Cl_2 (25 mL) over 10 min under N_2 at −40 °C. The resulting solution was slowly warmed to room temperature. After 20 min, TLC showed complete consumption of the starting material. Then, aqueous $NaHCO_3$ (30 mM, 33 mL) was added to neutralize the solution, and the products were separated from the CH_2Cl_2 into the aqueous layer. The aqueous layer was evaporated to dryness. The residue was purified on a silica column with 15% MeOH/CH_2Cl_2 as an eluent to afford an orange compound, DS-DN-BODIPY (43 mg, 29% yield). ^{1}H NMR (400 MHz, D_2O): δ 8.21 (d, J = 2.0 Hz, 1H), 8.20 (d, J = 8.4 Hz, 2H), 7.91 (dd, J = 8.4, 1.6 Hz, 1H), 2.62 (s, 6H), 1.54 (s, 6H). MS (ESI): calcd for $[M + Na]^+$, 641.00; found, 641.00.

Preparation and Characterization of Titania-Based Nanoparticles. Anatase TiO_2 nanoparticles (Ishihara Sangyo, A-100; 50−300 nm particles) were annealed at 500 °C for 2 h. The Au/TiO_2 particles (8 and 14 nm Au/TiO_2) were prepared by the deposition−precipitation method using $HAuCl_4$ and A-100 TiO_2 as the raw materials. Detailed descriptions of the morphology, crystal structure, and optical properties of the synthesized Au/TiO_2 particles are given in the literature.[23]

Instruments. Steady-state UV−visible absorption and fluorescence spectra were measured using UV−visible−NIR spectrophotometer (Shimadzu, UV-3100) and fluorescence spectrophotometer (HORIBA, FluoroMax-4). TEM measurements were performed using a JEOL EM-3000F instrument operating at 300 kV. FE-SEM measurements were performed using a JEOL JSM-6335F operating at 5 or 15 kV.

Bulk Photochemical Experiments. In a typical procedure, a TiO_2 dispersion (0.1 g L^{-1}) containing the probes (1 μM) was first sonicated for 2 min, and then transferred into a quartz cuvette. Prior to UV illumination, the suspension was purged with Ar gas for 10 min to completely remove the dissolved oxygen. After UV irradiation (Asahi Spectra, REX-120; 35 mW cm^{-1}), the samples were analyzed using the UV−visible absorption and fluorescence spectrometers. The details of the experimental and analytical procedures are described elsewhere.[21]

Single-Particle/Single-Molecule Fluorescence Measurements by Wide-Field Microscopy. The experimental setup was based on an Olympus IX81 inverted fluorescence microscope. The details of the experimental and analytical procedures are described elsewhere.[22,23] The experimental setup included an Olympus IX81 inverted fluorescence microscope. The 488 nm CW laser (OZ Optics; 0.1 kWcm^{-2} at the glass surface) and 365 nm LED (Opto-Line; 30 mW cm^{-2} at the glass surface) sources were used to excite the dyes and TiO_2, respectively. The transmission and emission images were recorded on an EMCCD camera (Roper Scientific, Evolve 512) at a frame rate of 20 frames s^{-1} using MetaMorph (Molecular Devices). Suitable dichroic mirrors and band-pass filters were used to improve the signal-to-noise ratio. All experimental data were obtained at room temperature. With the aim to determine the locations of the reactive site distributed on the surface, the precise positions of the fluorescent spots were analyzed for each image using the ImageJ software (http://rsb.info.nih.gov/ij/) and OriginPro 8.6 (OriginLab). A general approach is applied to define the intensity threshold in order to distinguish between the on and off states.[23,102] The threshold was chosen to be 3σ greater than the background noise levels. Counts above the threshold were then considered to be the fluorescence signal.

Single-Particle/Single-Molecule Fluorescence Measurements with Confocal Mcroscopy. Fluorescence lifetimes and spectra were recorded using an objective-scanning confocal microscope system (PicoQuant, MicroTime 200) coupled with an Olympus IX71 inverted fluorescence microscope.[22,23] The samples were excited through an oil-immersion objective lens (Olympus, UAPON 150XOTIRF; 1.45 NA, 150×) using a 485 nm pulsed laser (PicoQuant, LDH-D-C-485) controlled by a PDL-800B driver (PicoQuant). The emission from the sample was collected using the same objective and detected by a single-photon avalanche photodiode (Micro Photon Devices, PDM 50CT) through a dichroic mirror, a long-pass filter (Chroma, HQ510LP), a band-pass filter (Semrock, FF01-531/40-25), and a 50 μm pinhole for spatial filtering to reject out-of-focus signals. For the fluorescence spectral measurements, only the emission that passed through a long-pass filter and a slit entered the imaging spectrograph (ActonResearch, SP-2356) that was equipped with an electron-multiplying charge-coupled device (EMCCD) camera (Princeton Instruments, ProEM). The spectrum detected by the EM-CCD camera was stored and analyzed by using a personal computer. The spectra were typically integrated for 10 s. For the excitation spectral measurements, the samples were excited with a fiber-coupled pulsed laser (Spectra-Physics,

Mai Tai HTS-W provided with an automated frequency doubler, Inspire Blue FAST-W; 0.8 MHz repetition rate, 420−490 nm wavelength, 2.7 nm spectral width (full-width at half-maximum), 0.1 kW cm^{-2} at the glass surface) controlled by a PDL-800B driver (PicoQuant). The laser light was attenuated with a neutral density filter before coupled into a single-mode optical fiber. The optimum coupling efficiency was achieved and maintained by the automated laser beam alignment and stabilization system (TEM Messtechnik, Aligna). An instrument response function (IRF) of ~100 ps was obtained by measuring the scattered laser light in order to analyze the temporal profile. The emission was collected with the objective and detected by a single-photon avalanche photodiode (Micro Photon Devices, PDM 50CT) through a beam splitter (90% transmission, 10% reflection), a long-pass filter, a band-pass filter (Semrock, FF01-531/40-25), and a pinhole. All experimental data were obtained at room temperature.

Conflict of Interest: The authors declare no competing financial interest.

Acknowledgment. T.M. thanks the World Class University program funded by the Ministry of Education, Science and Technology through the National Research Foundation of Korea (R31-2011-000-10035-0) for the support. This work has been partly supported by Innovative Project for Advanced Instruments, Renovation Center of Instruments for Science Education and Technology, Osaka University, a Grant-in-Aid for Scientific Research (Projects 22245022 and others) from the Ministry of Education, Culture, Sports, Science and Technology (MEXT) of the Japanese Government, and The Murata Science Foundation.

Supporting Information Available: Experimental details including the additional results. This material is available free of charge *via* the Internet at http://pubs.acs.org.

REFERENCES AND NOTES

1. Achilefu, S. Introduction to Concepts and Strategies for Molecular Imaging. *Chem. Rev.* **2010**, *110*, 2575–2578.
2. de Silva, A. P.; Gunaratne, H. Q. N.; Gunnlaugsson, T.; Huxley, A. J. M.; McCoy, C. P.; Rademacher, J. T.; Rice, T. E. Signaling Recognition Events with Fluorescent Sensors and Switches. *Chem. Rev.* **1997**, *97*, 1515–1566.
3. Que, E. L.; Domaille, D. W.; Chang, C. J. Metals in Neurobiology: Probing Their Chemistry and Biology with Molecular Imaging. *Chem. Rev.* **2008**, *108*, 1517–1549.
4. Chalfie, M.; Tu, Y.; Euskirchen, G.; Ward, W. W.; Prasher, D. C. Green Fluorescent Protein as a Marker for Gene Expression. *Science* **1994**, *263*, 802–805.
5. Thomas, S. W., III; Joly, G. D.; Swager, T. M. Chemical Sensors Based on Amplifying Fluorescent Conjugated Polymers. *Chem. Rev.* **2007**, *107*, 1339–1386.
6. Kobayashi, H.; Ogawa, M.; Alford, R.; Choyke, P. L.; Urano, Y. New Strategies for Fluorescent Probe Design in Medical Diagnostic Imaging. *Chem. Rev.* **2010**, *110*, 2620–2640.
7. Martinez-Máñez, R.; Sancenón, F. Fluorogenic and Chromogenic Chemosensors and Reagents for Anions. *Chem. Rev.* **2003**, *103*, 4419–4476.
8. Weckhuysen, B. M. Chemical Imaging of Spatial Heterogeneities in Catalytic Solids at Different Length and Time Scales. *Angew. Chem., Int. Ed.* **2009**, *48*, 4910–4943.
9. De Cremer, G.; Sels, B. F.; De Vos, D. E.; Hofkens, J.; Roeffaers, M. B. J. Fluorescence Micro(spectro)scopy as a Tool To Study Catalytic Materials in Action. *Chem. Soc. Rev.* **2010**, *39*, 4703–4717.
10. Tachikawa, T.; Majima, T. Single-Molecule, Single-Particle Fluorescence Imaging of TiO_2-Based Photocatalytic Reactions. *Chem. Soc. Rev.* **2010**, *39*, 4802–4819.
11. Tachikawa, T.; Majima, T. Single-Molecule, Single-Particle Approaches for Exploring the Structure and Kinetics of Nanocatalysts. *Langmuir* **2012**, *28*, 8933–8943.
12. Buurmans, I. L. C.; Weckhuysen, B. M. Heterogeneities of Individual Catalyst Particles in Space and Time As Monitored by Spectroscopy. *Nat. Chem.* **2012**, *4*, 873–886.
13. Roeffaers, M. B. J.; Sels, B. F.; Loos, D.; Kohl, C.; Müllen, K.; Jacobs, P. A.; Hofkens, J.; De Vos, D. E. *In Situ* Space- and Time-Resolved Sorption Kinetics of Anionic Dyes on Individual LDH Crystals. *ChemPhysChem* **2005**, *6*, 2295–2299.
14. Roeffaers, M. B. J.; Sels, B. F.; Uji-i, H.; De Schryver, F. C.; Jacobs, P. A.; De Vos, D. E.; Hofkens, J. Spatially Resolved Observation of Crystal-Face-Dependent Catalysis by Single Turnover Counting. *Nature* **2006**, *439*, 572–575.
15. Xu, W.; Kong, J. S.; Yeh, Y.-T. E.; Chen, P. Single-Molecule Nanocatalysis Reveals Heterogeneous Reaction Pathways and Catalytic Dynamics. *Nat. Mater.* **2008**, *7*, 992–996.
16. Zhou, X.; Xu, W.; Liu, G.; Panda, D.; Chen, P. Size-Dependent Catalytic Activity and Dynamics of Gold Nanoparticles at the Single-Molecule Level. *J. Am. Chem. Soc.* **2010**, *132*, 138–146.
17. Han, K. S.; Liu, G.; Zhou, X.; Medina, R. E.; Chen, P. How Does a Single Pt Nanocatalyst Behave in Two Different Reactions? A Single-Molecule Study. *Nano Lett.* **2012**, *12*, 1253–1259.
18. Zhou, X.; Andoy, N. M.; Liu, G.; Choudhary, E.; Han, K.-S.; Shen, H.; Chen, P. Quantitative Super-Resolution Imaging Uncovers Reactivity Patterns on Single Nanocatalysts. *Nat. Nanotechnol.* **2012**, *7*, 237–241.
19. Xu, W.; Shen, H.; Kim, Y. J.; Zhou, X.; Liu, G.; Park, J.; Chen, P. Single-Molecule Electrocatalysis by Single-Walled Carbon Nanotubes. *Nano Lett.* **2009**, *9*, 3968–3973.
20. Naito, K.; Tachikawa, T.; Fujitsuka, M.; Majima, T. Single-Molecule Observation of Photocatalytic Reaction in TiO_2 Nanotube: Importance of Molecular Transport through Porous Structures. *J. Am. Chem. Soc.* **2009**, *131*, 934–936.
21. Tachikawa, T.; Wang, N.; Yamashita, S.; Cui, S.-C.; Majima, T. Design of a Highly Sensitive Fluorescent Probe for Interfacial Electron Transfer on a TiO_2 Surface. *Angew. Chem., Int. Ed.* **2010**, *49*, 8593–8597.
22. Tachikawa, T.; Yamashita, S.; Majima, T. Evidence for Crystal-Face-Dependent TiO_2 Photocatalysis from Single-Molecule Imaging and Kinetic Analysis. *J. Am. Chem. Soc.* **2011**, *133*, 7197–7204.
23. Wang, N.; Tachikawa, T.; Majima, T. Single-Molecule, Single-Particle Observation of Size-Dependent Photocatalytic Activity in Au/TiO_2 Nanocomposites. *Chem. Sci.* **2011**, *2*, 891–900.
24. Tachikawa, T.; Majima, T. Photocatalytic Oxidation Surfaces on Anatase TiO_2 Crystals Revealed by Single-Particle Chemiluminescence Imaging. *Chem. Commun.* **2012**, *48*, 3300–3302.
25. Xu, W.; Jain, P. K.; Beberwyck, B. J.; Alivisatos, A. P. Probing Redox Photocatalysis of Trapped Electrons and Holes on Single Sb-Doped Titania Nanorod Surfaces. *J. Am. Chem. Soc.* **2012**, *134*, 3946–3949.
26. Roeffaers, M. B. J.; De Cremer, G.; Libeert, J.; Ameloot, R.; Dedecker, P.; Bons, A.-J.; Bueckins, M.; Martens, J. A.; Sels, B. F.; De Vos, D. E.; *et al.* Super-Resolution Reactivity Mapping of Nanostructured Catalyst Particles. *Angew. Chem., Int. Ed.* **2009**, *48*, 9285–9289.
27. De Cremer, G.; Roeffaers, M. B. J.; Bartholomeeusen, E.; Lin, K.; Dedecker, P.; Pescarmona, P. P.; Jacobs, P. A.; De Vos, D. E.; Hofkens, J.; Sels, B. F. High-Resolution Single-Turnover Mapping Reveals Intraparticle Diffusion Limitation in Ti-MCM-41-Catalyzed Epoxidation. *Angew. Chem., Int. Ed.* **2010**, *49*, 908–911.
28. Loudet, A.; Burgess, K. BODIPY Dyes and Their Derivatives: Syntheses and Spectroscopic Properties. *Chem. Rev.* **2007**, *107*, 4891–4932.
29. Boens, N.; Leen, V.; Dehaen, W. Fluorescent Indicators Based on BODIPY. *Chem. Soc. Rev.* **2012**, *41*, 1130–1172.
30. Ferry, J. L.; Glaze, W. H. Photocatalytic Reduction of Nitro Organics over Illuminated Titanium Dioxide: Role of the TiO_2 Surface. *Langmuir* **1998**, *14*, 3551–3555.
31. Makarova, O. V.; Rajh, T.; Thurnauer, M. C.; Martin, A.; Kemme, P. A.; Cropek, D. Surface Modification of TiO_2 Nanoparticles for Photochemical Reduction of Nitrobenzene. *Environ. Sci. Technol.* **2000**, *34*, 4797–4803.

32. Tada, H.; Ishida, T.; Takao, A.; Ito, S. Drastic Enhancement of TiO_2-Photocatalyzed Reduction of Nitrobenzene by Loading Ag Clusters. *Langmuir* **2004**, *20*, 7898–7900.
33. Hervés, P.; Pérez-Lorenzo, M.; Liz-Marzán, L. M.; Dzubiella, J.; Lu, Y.; Ballauff, M. Catalysis by Metallic Nanoparticles in Aqueous Solution: Model Reactions. *Chem. Soc. Rev.* **2012**, *41*, 5577–5587.
34. Fujishima, A.; Rao, T. N.; Tryk, D. A. Titanium Dioxide Photocatalysis. *J. Photochem. Photobiol., C* **2000**, *1*, 1–21.
35. Thompson, T. L.; Yates, J. T., Jr. Surface Science Studies of the Photoactivation of TiO_2-New Photochemical Processes. *Chem. Rev.* **2006**, *106*, 4428–4453.
36. Chen, X.; Mao, S. S. Titanium Dioxide Nanomaterials: Synthesis, Properties, Modifications, and Applications. *Chem. Rev.* **2007**, *107*, 2891–2959.
37. Tachikawa, T.; Fujitsuka, M.; Majima, T. Mechanistic Insight into the TiO_2 Photocatalytic Reactions: Design of New Photocatalysts. *J. Phys. Chem. C* **2007**, *111*, 5259–5275.
38. Kamat, P. V. Meeting the Clean Energy Demand: Nanostructure Architectures for Solar Energy Conversion. *J. Phys. Chem. C* **2007**, *111*, 2834–2860.
39. Kudo, A.; Miseki, Y. Heterogeneous Photocatalyst Materials for Water Splitting. *Chem. Soc. Rev.* **2009**, *38*, 253–278.
40. Chen, X.; Shen, S.; Guo, L.; Mao, S. S. Semiconductor-Based Photocatalytic Hydrogen Generation. *Chem. Rev.* **2010**, *110*, 6503–6570.
41. Schrauben, J. N.; Hayoun, R.; Valdez, C. N.; Braten, M.; Fridley, L.; Mayer, J. M. Titanium and Zinc Oxide Nanoparticles Are Proton-Coupled Electron Transfer Agents. *Science* **2012**, *336*, 1298–1301.
42. Karolin, J.; Johansson, L. B. A.; Strandberg, L.; Ny, T. Fluorescence and Absorption Spectroscopic Properties of Dipyrrometheneboron Difluoride (BODIPY) Derivatives in Liquids, Lipid Membranes, and Proteins. *J. Am. Chem. Soc.* **1994**, *116*, 7801–7806.
43. Urano, Y.; Asanuma, D.; Hama, Y.; Koyama, Y.; Barrett, T.; Kamiya, M.; Nagano, T.; Watanabe, T.; Hasegawa, A.; Choyke, P. L.; *et al.* Selective Molecular Imaging of Viable Cancer Cells with pH-Activatable Fluorescence Probes. *Nat. Med.* **2009**, *15*, 104–109.
44. Dung, D.; Ramsden, J.; Grätzel, M. Dynamics of Interfacial Electron-Transfer Processes in Colloidal Semiconductor Systems. *J. Am. Chem. Soc.* **1982**, *104*, 2977–2985.
45. Kosmulski, M. The Significance of the Difference in the Point of Zero Charge between Rutile and Anatase. *Adv. Colloid Interface Sci.* **2002**, *99*, 255–264.
46. Hiemstra, T.; van Riemsdijk, W. H. A Surface Structural Approach to Ion Adsorption: The Charge Distribution (CD) Model. *J. Colloid Interface Sci.* **1996**, *179*, 488–508.
47. Bourikas, K.; Stylidi, M.; Kondarides, D. I.; Verykios, X. E. Adsorption of Acid Orange 7 on the Surface of Titanium Dioxide. *Langmuir* **2005**, *21*, 9222–9230.
48. O'Rourke, C.; Mills, A. Adsorption and Photocatalytic Bleaching of Acid Orange 7 on P25 Titania. *J. Photochem. Photobiol., A* **2010**, *216*, 261–267.
49. Because the potential of the reduction of phenylhydroxylamine to aniline is more negative than that of the reduction of nitrobenzene to phenylhydroxylamine, the successive reduction of HN-BODIPY would be minor.[21]
50. The shape of the fluorescence excitation spectra remained unchanged during UV irradiation and was nearly identical to the absorption spectrum of the purified fluorescent product, implying that there was only one fluorescent product (Figure S3, Supporting Information).
51. Obee, T. N.; Brown, R. T. TiO_2 Photocatalysis for Indoor Air Applications: Effects of Humidity and Trace Contaminant Levels on the Oxidation Rates of Formaldehyde, Toluene, and 1,3-Butadiene. *Environ. Sci. Technol.* **1995**, *29*, 1223–1231.
52. Nosaka, A. Y.; Fujiwara, T.; Yagi, H.; Akutsu, H.; Nosaka, Y. Photocatalytic Reaction Sites at the TiO_2 Surface as Studied by Solid-State ^{1}H NMR Spectroscopy. *Langmuir* **2003**, *19*, 1935–1937.
53. The intensity-weighted average fluorescence lifetime of the products generated during UV irradiation of a single TiO_2 particle was about 0.5 ns, which is much shorter than that (3.7 ns) of DS-HN-BODIPY in the bulk solution. This significant fluorescence quenching is mainly due to an interfacial ET from the excited BODIPY chromophore to the CB of TiO_2.[21]
54. Andreussi, O.; Corni, S.; Mennucci, B.; Tomasi, J. Radiative and Nonradiative Decay Rates of a Molecule Close to a Metal Particle of Complex Shape. *J. Chem. Phys.* **2004**, *121*, 10190–10202.
55. Lakowicz, J. R. Radiative Decay Engineering 5: Metal-Enhanced Fluorescence and Plasmon Emission. *Anal. Biochem.* **2005**, *337*, 171–194.
56. Cannone, F.; Chirico, G.; Bizzarri, A. R.; Cannistraro, S. Quenching and Blinking of Fluorescence of a Single Dye Molecule Bound to Gold Nanoparticles. *J. Phys. Chem. B* **2006**, *110*, 16491–16498.
57. Carminati, R.; Greffet, J. J.; Henkel, C.; Vigoureux, J. M. Radiative and Non-radiative Decay of a Single Molecule Close to a Metallic Nanoparticle. *Opt. Commun.* **2006**, *261*, 368–375.
58. Tam, F.; Goodrich, G. P.; Johnson, B. R.; Halas, N. J. Plasmonic Enhancement of Molecular Fluorescence. *Nano Lett.* **2007**, *7*, 496–501.
59. Chen, Y.; Munechika, K.; Ginger, D. S. Dependence of Fluorescence Intensity on the Spectral Overlap between Fluorophores and Plasmon Resonant Single Silver Nanoparticles. *Nano Lett.* **2007**, *7*, 690–696.
60. Munechika, K.; Chen, Y.-C.; Tillack, A. F.; Kulkarni, A. P.; Jen-La Plante, I.; Munro, A. M.; Ginger, D. S. Quantum Dot/Plasmonic Nanoparticle Metachromophores with Quantum Yields That Vary with Excitation Wavelength. *Nano Lett.* **2011**, *11*, 2725–2730.
61. Kuhn, S.; Hakanson, U.; Rogobete, L.; Sandoghdar, V. Enhancement of Single-Molecule Fluorescence Using a Gold Nanoparticle as an Optical Nanoantenna. *Phys. Rev. Lett.* **2006**, *97*, 017402/1–017402/4.
62. Bharadwaj, P.; Novotny, L. Spectral Dependence of Single Molecule Fluorescence Enhancement. *Opt. Express* **2007**, *15*, 14266–14274.
63. Barnes, W. L. Fluorescence near Interfaces: The Role of Photonic Mode Density. *J. Mod. Opt.* **1998**, *45*, 661–699.
64. Masiello, D. J.; Schatz, G. C. On the Linear Response and Scattering of an Interacting Molecule−Metal System. *J. Chem. Phys.* **2010**, *132*, 064102/1–064102/8.
65. Weber, W. H.; Eagen, C. F. Energy Transfer from an Excited Dye Molecule to the Surface Plasmons of an Adjacent Metal. *Opt. Lett.* **1979**, *4*, 236–238.
66. Gersten, J.; Nitzan, A. Spectroscopic Properties of Molecules Interacting with Small Dielectric Particles. *J. Chem. Phys.* **1981**, *75*, 1139–1152.
67. Yun, C. S.; Javier, A.; Jennings, T.; Fisher, M.; Hira, S.; Peterson, S.; Hopkins, B.; Reich, N. O.; Strouse, G. F. Nanometal Surface Energy Transfer in Optical Rulers, Breaking the FRET Barrier. *J. Am. Chem. Soc.* **2005**, *127*, 3115–3119.
68. Jennings, T. L.; Singh, M. P.; Strouse, G. F. Fluorescent Lifetime Quenching near $d = 1.5$ nm Gold Nanoparticles: Probing NSET Validity. *J. Am. Chem. Soc.* **2006**, *128*, 5462–5467.
69. Seelig, J.; Leslie, K.; Renn, A.; Kühn, S.; Jacobsen, V.; Van de Corput, M.; Wyman, C.; Sandoghdar, V. Nanoparticle-Induced Fluorescence Lifetime Modification as Nanoscopic Ruler: Demonstration at the Single Molecule Level. *Nano Lett.* **2007**, *7*, 685–689.
70. Another possible reason for the fluorescence quenching is the photoinduced electron transfer from the excited dye to or from the Au nanoparticles.[71−73] This process may become more favorable in polar solvents when the dyes are very close to the Au nanopartilce (typically within 1 nm).
71. Ipe, B. I.; Thomas, K. G.; Barazzouk, S.; Hotchandani, S.; Kamat, P. V. Photoinduced Charge Separation in a Fluorophore-Gold Nanoassembly. *J. Phys. Chem. B* **2002**, *106*, 18–21.

72. Kamat, P. V.; Barazzouk, S.; Hotchandani, S. Electrochemical Modulation of Fluorophore Emission on a Nanostructured Gold Film. *Angew. Chem., Int. Ed.* **2002**, *41*, 2764–2767.
73. Devadas, M. S.; Kwak, K.; Park, J.-W.; Choi, J.-H.; Jun, C.-H.; Sinn, E.; Ramakrishna, G.; Lee, D. Directional Electron Transfer in Chromophore-Labeled Quantum-Sized Au_{25} Clusters: Au_{25} as an Electron Donor. *J. Phys. Chem. Lett.* **2010**, *1*, 1497–1503.
74. Primo, A.; Corma, A.; García, H. Titania Supported Gold Nanoparticles as Photocatalyst. *Phys. Chem. Chem. Phys.* **2011**, *13*, 886–910.
75. Linic, S.; Christopher, P.; Ingram, D. B. Plasmonic-Metal Nanostructures for Efficient Conversion of Solar to Chemical Energy. *Nat. Mater.* **2011**, *10*, 911–921.
76. Yen, C.-W.; El-Sayed, M. A. Plasmonic Field Effect on the Hexacyanoferrate (III)-Thiosulfate Electron Transfer Catalytic Reaction on Gold Nanoparticles: Electromagnetic or Thermal? *J. Phys. Chem. C* **2009**, *113*, 19585–19590.
77. Adleman, J. R.; Boyd, D. A.; Goodwin, D. G.; Psaltis, D. Heterogeneous Catalysis Mediated by Plasmon Heating. *Nano Lett.* **2009**, *9*, 4417–4423.
78. Chen, X.; Zhu, H.-Y.; Zhao, J.-C.; Zheng, Z.-F.; Gao, X.-P. Visible-Light-Driven Oxidation of Organic Contaminants in Air with Gold Nanoparticle Catalysts on Oxide Supports. *Angew. Chem., Int. Ed.* **2008**, *47*, 5353–5356.
79. Tian, Y.; Tatsuma, T. Mechanisms and Applications of Plasmon-Induced Charge Separation at TiO_2 Films Loaded with Gold Nanoparticles. *J. Am. Chem. Soc.* **2005**, *127*, 7632–7637.
80. Du, L.; Furube, A.; Yamamoto, K.; Hara, K.; Katoh, R.; Tachiya, M. Plasmon-Induced Charge Separation and Recombination Dynamics in Gold−TiO_2 Nanoparticle Systems: Dependence on TiO_2 Particle Size. *J. Phys. Chem. C* **2009**, *113*, 6454–6462.
81. Sakai, N.; Fujiwara, Y.; Takahashi, Y.; Tatsuma, T. Plasmon-Resonance-Based Generation of Cathodic Photocurrent at Electrodeposited Gold Nanoparticles Coated with TiO_2 Films. *ChemPhysChem* **2009**, *10*, 766–769.
82. Kowalska, E.; Mahaney, O. O. P.; Abe, R.; Ohtani, B. Visible-Light-Induced Photocatalysis through Surface Plasmon Excitation of Gold on Titania Surfaces. *Phys. Chem. Chem. Phys.* **2010**, *12*, 2344–2355.
83. Gomes Silva, C.; Juárez, R.; Marino, T.; Molinari, R.; García, H. Influence of Excitation Wavelength (UV or Visible Light) on the Photocatalytic Activity of Titania Containing Gold Nanoparticles for the Generation of Hydrogen or Oxygen from Water. *J. Am. Chem. Soc.* **2011**, *133*, 595–602.
84. Naya, S.; Inoue, A.; Tada, H. Visible-Light Activity Enhancement of Gold-Nanoparticle-Loaded Titanium(IV) Dioxide by Preferential Excitation of Localized Surface Plasmon Resonance. *ChemPhysChem* **2011**, *12*, 2719–2723.
85. Awazu, K.; Fujimaki, M.; Rockstuhl, C.; Tominaga, J.; Murakami, H.; Ohki, Y.; Yoshida, N.; Watanabe, T. A Plasmonic Photocatalyst Consisting of Silver Nanoparticles Embedded in Titanium Dioxide. *J. Am. Chem. Soc.* **2008**, *130*, 1676–1680.
86. Ingram, D. B.; Linic, S. Water Splitting on Composite Plasmonic-Metal/Semiconductor Photoelectrodes: Evidence for Selective Plasmon-Induced Formation of Charge Carriers near the Semiconductor Surface. *J. Am. Chem. Soc.* **2011**, *133*, 5202–5205.
87. Liu, Z.; Hou, W.; Pavaskar, P.; Aykol, M.; Cronin, S. B. Plasmon Resonant Enhancement of Photocatalytic Water Splitting under Visible Illumination. *Nano Lett.* **2011**, *11*, 1111–1116.
88. Chen, J.-J.; Wu, J. C. S.; Wu, P. C.; Tsai, D. P. Plasmonic Photocatalyst for H_2 Evolution in Photocatalytic Water Splitting. *J. Phys. Chem. C* **2011**, *115*, 210–216.
89. Seh, Z. W.; Liu, S.; Low, M.; Zhang, S.-Y.; Liu, Z.; Mlayah, A.; Han, M.-Y. Janus Au−TiO_2 Photocatalysts with Strong Localization of Plasmonic Near-Fields for Efficient Visible-Light Hydrogen Generation. *Adv. Mater.* **2012**, *24*, 2310–2314.
90. Atomic force microscopy (AFM) experiments showed no obvious change in Au particle size before and after photoirradiation. This result suggests that the fragmentation of the Au nanoparticles under photoirradiation was likely negligible under the present experimental conditions.[23]
91. Zhang, Z.; Yates, J. T., Jr. Band Bending in Semiconductors: Chemical and Physical Consequences at Surfaces and Interfaces. *Chem. Rev.* **2012**, *112*, 5520–5551.
92. Chen, H. M.; Chen, C. K.; Chen, C.-J.; Cheng, L.-C.; Wu, P. C.; Cheng, B. H.; Ho, Y. Z.; Tseng, M. L.; Hsu, Y.-Y.; Chan, T.-S.; *et al.* Plasmon Inducing Effects for Enhanced Photoelectrochemical Water Splitting: X-ray Absorption Approach to Electronic Structures. *ACS Nano* **2012**, *6*, 7362–7372.
93. Serpone, N. Is the Band Gap of Pristine TiO_2 Narrowed by Anion- and Cation-Doping of Titanium Dioxide in Second-Generation Photocatalysts?. *J. Phys. Chem. B* **2006**, *110*, 24287–24293.
94. Di Valentin, C.; Pacchioni, G.; Selloni, A. Reduced and n-Type Doped TiO_2: Nature of Ti^{3+} Species. *J. Phys. Chem. C* **2009**, *113*, 20543–20552.
95. Frank, A. J.; Kopidakis, N.; van de Lagemaat, J. Electrons in Nanostructured TiO_2 Solar Cells: Transport, Recombination and Photovoltaic Properties. *Coord. Chem. Rev.* **2004**, *248*, 1165–1179.
96. Zürner, A.; Kirstein, J.; Döblinger, M.; Bräuchle, C.; Bein, T. Visualizing Single-Molecule Diffusion in Mesoporous Materials. *Nature* **2007**, *450*, 705–708.
97. Dukes, M. J.; Peckys, D. B.; de Jonge, N. Correlative Fluorescence Microscopy and Scanning Transmission Electron Microscopy of Quantum-Dot-Labeled Proteins in Whole Cells in Liquid. *ACS Nano* **2010**, *4*, 4110–4116.
98. Pan, D.; Hu, D.; Lu, H. P. Probing Inhomogeneous Vibrational Reorganization Energy Barriers of Interfacial Electron Transfer. *J. Phys. Chem. B* **2005**, *109*, 16390–16395.
99. Sevinc, P. C.; Wang, X.; Wang, Y.; Zhang, D.; Meixner, A. J.; Lu, H. P. Simultaneous Spectroscopic and Topographic Near-Field Imaging of TiO_2 Single Surface States and Interfacial Electronic Coupling. *Nano Lett.* **2011**, *11*, 1490–1494.
100. van Schrojenstein Lantman, E. M.; Deckert-Gaudig, T.; Mank, A. J. G.; Deckert, V.; Weckhuysen, B. M. Catalytic Processes Monitored at the Nanoscale with Tip-Enhanced Raman Spectroscopy. *Nat. Nanotechnol.* **2012**, *7*, 583–586.
101. Li, L.; Han, J.; Nguyen, B.; Burgess, K. Syntheses and Spectral Properties of Functionalized, Water-Soluble BODIPY Derivatives. *J. Org. Chem.* **2008**, *73*, 1963–1970.
102. Kuno, M.; Fromm, D. P.; Hamann, H. F.; Gallagher, A.; Nesbitt, D. J. "On"/"Off" Fluorescence Intermittency of Single Semiconductor Quantum Dots. *J. Chem. Phys.* **2001**, *115*, 1028–1040.